



## Lidar measurements of wake around a bridge deck

Mohammad Nafisifard <sup>a,\*</sup>, Jasna B. Jakobsen <sup>a</sup>, Jonas T. Snæbjörnsson <sup>b</sup>, Mikael Sjöholm <sup>c</sup>, Jakob Mann <sup>c</sup>

<sup>a</sup> Department of Mechanical and Structural Engineering and Material Science, University of Stavanger, Stavanger, Norway

<sup>b</sup> Department of Engineering, Reykjavík University, Reykjavík, Iceland

<sup>c</sup> Department of Wind and Energy Systems, Technical University of Denmark, Roskilde, Denmark

### ARTICLE INFO

**Keywords:**

Wind lidar measurement  
Turbulence  
Full-scale  
Suspension bridge  
Wake measurements

### ABSTRACT

Remote wind sensing technologies allow for measurements in a spatial domain beyond the one accessible by anemometers fixed to a mast. Remote optical wind sensors installed at an existing bridge site can both provide new information on the wind flow upstream of the bridge and capture the disturbed flow around the structure. These possibilities are explored in the presented measurement campaign with three synchronised continuous-wave Doppler lidars at the Lysefjord bridge in Norway. In particular, the interaction between the oncoming wind flow and the bridge deck is studied in terms of the mean velocity deficit wake profile as well as the spectral turbulence characteristics. The lidar measurements are validated by comparing the lidar observations at locations undisturbed by the structure with corresponding sonic anemometer data recorded 6 m and 10 m above the deck. The consistency between the two sets of data is tested in terms of the turbulence time series, their spectral content and the statistical moments. Within the wake of the bridge, significant values of vertical velocity and inclination angles, as well as turbulence intensities are seen. Moreover, the wake region can be distinguished by its singular spectral content, cross-correlation coefficient, and coherence. The results show that the tailored configuration of the lidars succeeded in providing information on 3D turbulence around the bridge, thereby capturing the bridge aerodynamic characteristics in full-scale.

## 1. Introduction

Several long-span bridges are currently built or planned across several fjords in Norway as part of the Coastal Highway Route E39 project. These slender structures are vulnerable to wind loading generated by atmospheric turbulence (Lu et al., 2020) and are strongly influenced by the local terrain (Cheynet et al., 2020; Lange et al., 2016). Constructing a long-span bridge in a complex terrain requires detailed knowledge of the local wind conditions to accurately predict the design wind loads, which are among the governing design factors (Cheynet et al., 2016a). The wind gust loading on bridge decks requires knowledge of the three-dimensional turbulence, including its correlation (coherence) along the bridge span (Miyata et al., 2002; Toriumi et al., 2000). The fluctuating wind field translates into fluctuating wind forces (drag, lift, and overturning moment) as the natural wind interacts with the bridge deck as a so-called bluff body (Cheynet et al., 2016a; Tamura and Kareem, 2013). Furthermore, some of the novel bridge designs

proposed are susceptible to wind and turbulence properties not generally included in studies of bridge aerodynamics (Zhang et al., 2022).

Bridge aerodynamics is studied in wind tunnels by testing a bridge deck section model (Chen et al., 2014; Yang et al., 2015; Nafisifard et al., 2023a). Numerical flow simulations around a bridge girder section (Kuroda, 1997) are also performed, providing more details of the flow structures around the deck. Both approaches normally focus on investigating the case when the idealised flow direction is perpendicular to the bridge girder section. In full-scale, however, the local mean wind direction is not necessarily perpendicular to the main bridge axis; it may also have non-uniform characteristics along the bridge span and appear in a non-stationary manner. The discrepancies between the Reynolds numbers attainable in wind tunnels and numerical models versus those in full-scale can also contribute to differences in the wind-structure interaction observed at the different scales. Studying bridge aerodynamics in full-scale is thus of great importance to reduce uncertainties in wind load modelling.

\* Corresponding author.

E-mail addresses: [mohammad.nafisifard@uis.no](mailto:mohammad.nafisifard@uis.no) (M. Nafisifard), [jasna.b.jakobsen@uis.no](mailto:jasna.b.jakobsen@uis.no) (J.B. Jakobsen), [jonasthor@ru.is](mailto:jonasthor@ru.is) (J.T. Snæbjörnsson), [misj@dtu.dk](mailto:misj@dtu.dk) (M. Sjöholm), [jmsq@dtu.dk](mailto:jmsq@dtu.dk) (J. Mann).

Due to a range of practical challenges associated with field measurements, only a limited number of studies have been devoted to the direct observations of full-scale bridge aerodynamics. Those include surface pressure measurements and recordings by sonic anemometers installed on the bridge, both above the deck and in the disturbed flow regions close to the bridge deck (Daniotti, 2022; Li et al., 2014). A novel approach utilising optical remote wind sensing, with two continuous-wave lidars (light detection and ranging) installed on the bridge, was introduced in Cheynet et al. (2016b, 2017a), Nafisifard et al. (2021). The two synchronised lidars were overlooking the bridge deck wake as well as the horizontal incoming flow at the bridge site, allowing the estimation of the horizontal wind coherence. The optical wind sensors were integrated in a WindScanner system developed by the Technical University of Denmark. As demonstrated in that study, remote wind sensing using wind lidars, free of flow distortions by a supporting mast (Cheynet et al., 2019), has a promising potential to gather complementary wind data in previously inaccessible areas across deep fjords and can thereby contribute to an improved bridge design basis. In this way, the data collected by conventional in-situ sensors (anemometers) can be related to the actual flow conditions present along the bridge span. Both pulsed lidars and continuous-wave lidars are applicable for use in bridge engineering. Pulsed lidars can simultaneously monitor airflow at multiple distances, up to a few kilometres (Cheynet et al., 2017b, 2017c). However, a relatively low temporal (1 s) and spatial resolution (e.g., 25–100 m) limit the observations to the low-frequency flow components, such as the mean wind velocity. A continuous-wave lidar monitors the flow with a considerably larger sampling frequency (up to 400 Hz) and a higher spatial resolution than a pulsed lidar, but the largest scanning distances are limited to a few hundred meters. The scanning lidars, equipped with a rotating scanning head, provide additional flexibility in selecting the measurement domain, favouring flow investigations in bridge engineering (Cheynet et al., 2016b, 2017a; Nafisifard et al., 2021, 2023b; Nafisifard et al., 2023c). The more complex systems can simultaneously integrate several time-synchronised scanning lidars to monitor specified scanning patterns. Since around 2000, commercial wind lidars have been increasingly applied in wind energy and other engineering fields (Mikkelsen et al., 2017). The lidars have reduced in price and their operational reliability has increased over the last decade. In the wind energy industry, vertical lidar profilers, short- and long-range scanning lidars, and nacelle-mounted lidars are commonly used (Fu et al., 2022; Guo et al., 2022; Sebastiani et al., 2022; Puccioni et al., 2023). Other applications of remote sensing are currently being developed, for the design of civil engineering structures, in urban wind engineering, aviation (Angelou et al., 2021), etc.

The above-mentioned dual lidar measurements from a suspension bridge (Cheynet et al., 2016b, 2017a; Nafisifard et al., 2021) were restricted to a single plane at each time instant, allowing only the characterisation of two simultaneous velocity components, primarily in the horizontal plane. To overcome this limitation and enable the observations of the vertical turbulence, which governs both the vertical and the twisting response of the bridge girder, the present investigation adds a new dimension to the previous lidar measurement setup by integrating the third continuous wave lidar into the WindScanner system, for novel measurement of the 3D turbulence around the bridge. The selected configuration of the lidars in this campaign makes it possible to resolve the three-dimensional turbulence components with considerable accuracy over vast measurement domains depending on the scanning pattern. The results derived from the lidar measurements are validated through comparison with corresponding data from sonic anemometers. The measurement campaign addresses the overall research question: How can lidars be applied to obtain new information on wind conditions relevant for bridge design? Or more specifically: How can lidars provide new information on wind-structure interaction in full-scale?

The paper is structured as follows: The measurement site and the long-term instrumentation on the bridge are introduced in Section 2,

together with the description of the lidar measurement configuration and the adopted scanning patterns. Section 3 presents the lidar data processing required to determine the line-of-sight (LOS) velocities and the three instantaneous wind components. Various turbulence statistical parameters relevant to the wind load estimation are also introduced. Section 4 discusses the characteristics of the bridge deck wake, in terms of the mean velocity and direction profiles, profiles of the turbulence intensity and the turbulence cross-spectra. The force coefficients associated with the observed velocity deficit are also estimated. Finally, the main findings and conclusions of the measurement campaign are discussed and summarised in Section 5.

## 2. Measurement site and monitoring setup

### 2.1. The case study: Lysefjord bridge

The Lysefjord bridge is a suspension bridge constructed in 1997 at the inlet of a Norwegian fjord with a main span of 446 m and a deck height of 2.76 m while the deck width is 12.3 m consisting of two traffic lanes and one pedestrian path (Fig. 1). At the midspan, the bridge is positioned 55 m above sea level (Fig. 1b). The bridge axis is aligned at an angle of 42° from North, giving North-West to South-East orientation of the bridge (Fig. 1c). The two dominant wind directions follow the fjord alignment, as observed by the sonic anemometers on the bridge and reported by Snæbjörnsson et al. (2017). The flow from inside the fjord (from N-NE) is, to a higher degree, influenced by the topography and, on average, more turbulent compared to the flow from the outside of the fjord (from the south-southwest), which is usually stronger, coming from a more open area. That makes the Lysefjord bridge an interesting case to study wind conditions in a complex terrain.

### 2.2. Long-term instrumentation: sonic anemometry

Since 2013, the bridge has been extensively instrumented by sensors for turbulence and vibration monitoring. The atmospheric instrumentation consists of ten 3D sonic anemometers (WindMasterPro with a sampling frequency of 32 Hz, manufactured by Gill Instruments Ltd.) and one weather station (2D Weather Transmitter with a sampling frequency of 4 Hz, manufactured by Vaisala). The weather station records the horizontal wind components, as well as relative humidity, barometric pressure and temperature. The individual sensors are visualised in Fig. 2d with their associated ID. The first letter of the ID indicates the sensor location, either on a hanger (denoted by H) or the deck (denoted by D, with a sensor head 2 m from the deck leading/trailing edge). The subsequent two digits specify the hanger number, followed by the letter W and E, for the west and east side of the deck, respectively. All the hanger sonics are installed 6 m above the road surface except one, which is mounted 10 m above the deck, as marked by the additional letter "t". A master data acquisition unit inside the bridge collects data from four distributed data acquisition units linked to the different sensors. GPS antennas provide time synchronisation. The data are sampled at 50 Hz and transferred via 4G network to a server at the University of Stavanger.

### 2.3. Short-term instrumentation: WindScanner system

The wind field around the bridge deck was examined using three synchronised continuous-wave lidars, also called WindScanners (Fig. 3), provided by the Technical University of Denmark (DTU). Two lidars were deployed on the bridge deck walkaway on the west side, namely R2D1 and R2D2. The distance between them was 36 m, which corresponds to three times the distance between hangers, and they were each located 18 m from hanger 5, which is 67 m from the north tower. The position of the deck lidars was adopted as a compromise between two competing requirements. One favours a larger distance from the tower for flow measurements unaffected by the fjord cliffs and the tower. The

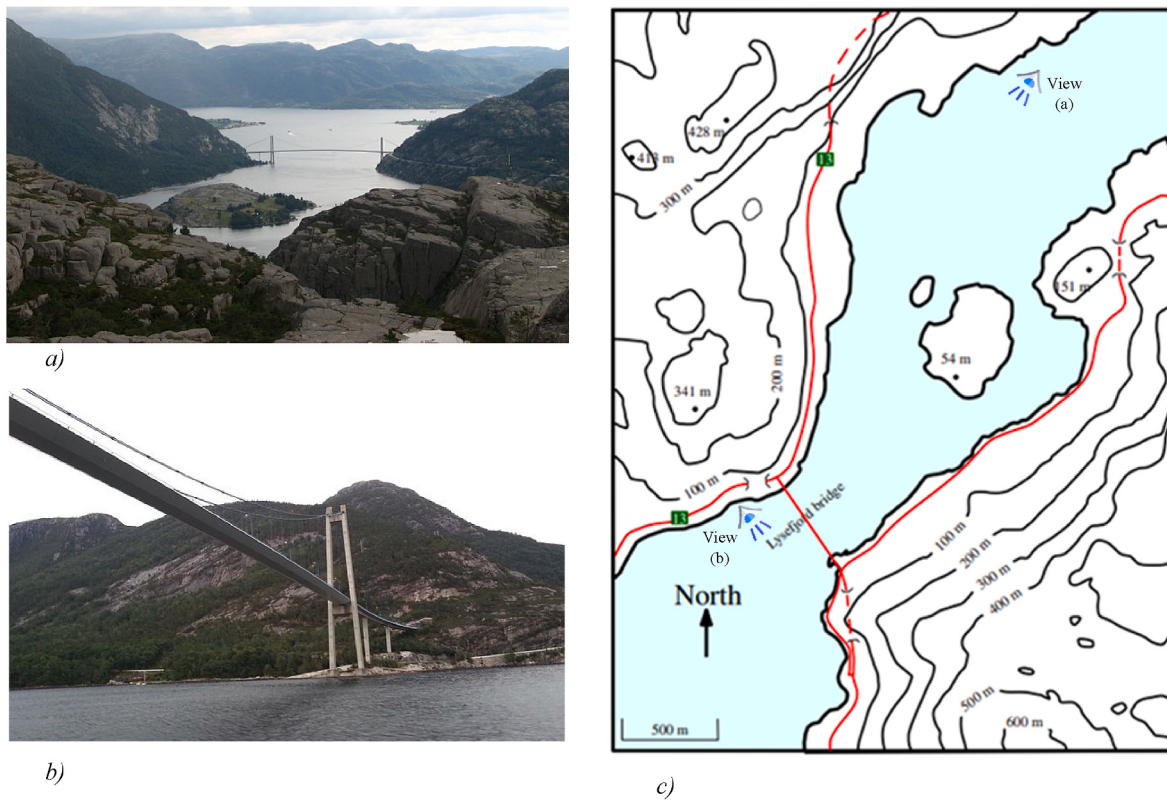


**Fig. 1.** Different views of Lysefjord bridge. a) From the east (from Wikimedia commons). b) From the ground at the North (from Wikimedia commons). c) Topographic map with view points ([Cheynet et al., 2019](#)).

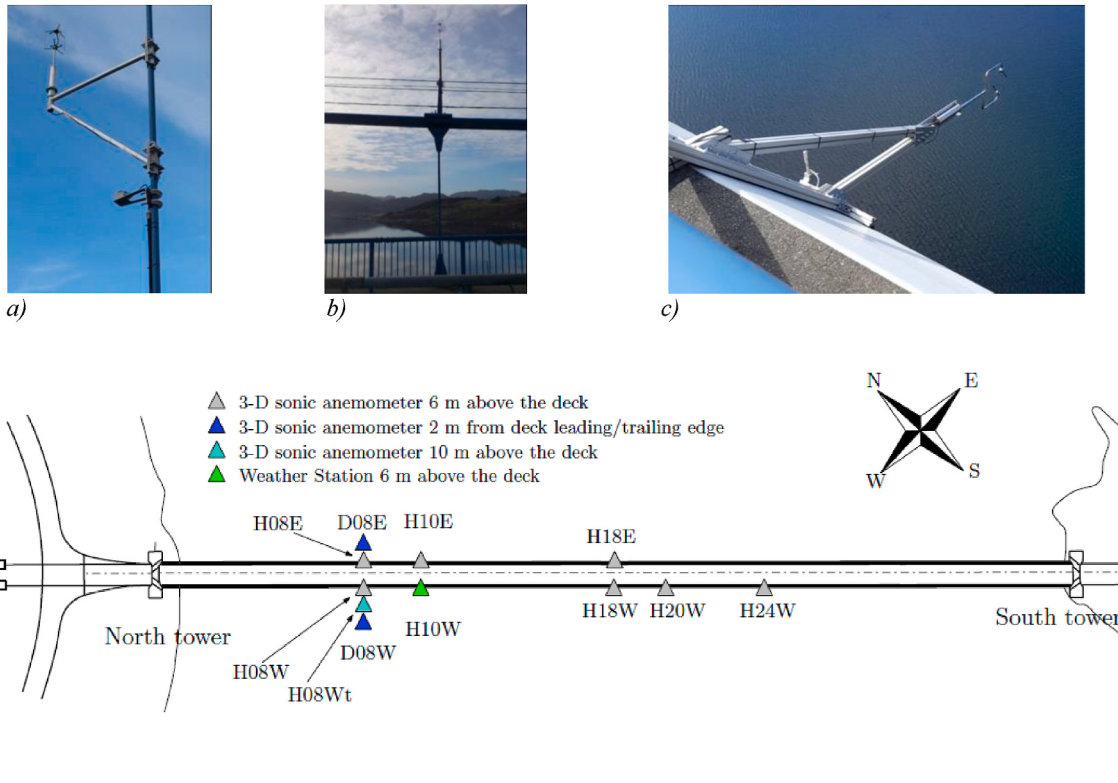


**Fig. 2.** Long-term sonic anemometers instrumentation at Lysefjord bridge for wind turbulence measurements. Two neighbouring hangers have 12 m distance ([Cheynet et al., 2019](#)). a) H08Wt. b) H18E. c) D08W. d) Sonic layout.

other one favours a shorter distance from the tower to limit the sampling

volumes of the lidar at the tower foundation. The adopted distance



**Fig. 3.** Lidar measurement setup, showing a view of the installed lidars. a) Deck lidar R2D1. b) Deck lidar R2D2. c) Ground lidar R2D3.

between the two lidars, corresponding to approximately three bridge deck widths, facilitated measurements with relatively small sampling volumes in the vicinity of the bridge deck. The third lidar (R2D3) was installed 38 m below the bridge deck, next to the North tower foundation, on a dedicated platform built for the measurements. It was positioned 10.5 m away from the vertical plane defined by the two lidars on the bridge deck.

All three lidars have a 3-inch-wide optical telescope and a rotating double-prism head, allowing for scanning within a cone with a half-opening angle of  $61^\circ$ . The key technical properties of the lidars are reported in Table 1 based on the detailed information provided in (Sjöholm et al., 2014) on the modified lidar instruments. The WindScanner lidar system synchronises the LOS measurements by the three lidar units, targeting a common steerable measurement “point” at all times.

### 2.3.1. Scanning patterns

The lidar measurement setup with the bridge and wind-based coordinate systems is shown in Fig. 4. The origin of the coordinate system is located at the bottom cap of the hanger 5. The figure also illustrates the three scanning patterns studied, which consist of two lines, a vertical and a horizontal, along with a bowtie-like pattern. For most of the campaign, the patterns were run in a cyclic schedule and the measurements during the pattern switching (about a second every 20 min) are disregarded from the subsequent analysis.

**2.3.1.1. Vertical and horizontal parallel line.** Flow conditions in the vicinity of the bridge deck are monitored along a vertical and a horizontal line parallel to the bridge axis, each 20 m long. The scanning lines are separated from the nose of the bridge deck by 11 m, a distance comparable to the total width of the deck,  $B = 12.3$  m, and centred 0.74 m above the deck road surface. Both lines are centred in front of hanger 5, in between the two deck lidars. Each cycle along a single scanning line, in both directions, takes half a second, containing ca. 161 data points. The position of the measurement volumes along the scanning line follows a smoothed triangular wave function of time, as illustrated in Fig. 5. The peak and the trough of the waveform have a constant sampling frequency of 2 Hz. In contrast, other locations along the scanning line are revisited with two different, alternating time steps, except at the central part of the scanning line where the time step is fixed to 0.25 s, i.e.

the sampling frequency is 4 Hz.

**2.3.1.2. Bowtie-like pattern.** The measurement domain is represented by a bowtie-like scanning pattern in a vertical plane separated from the nose of the bridge deck by 39 m, corresponding to 3.2 B. The horizontal and vertical segments of the scanning pattern are 80 m and 60 m long, respectively. The measurement data along the bowtie-like pattern are acquired with a sampling rate of 322.6 Hz. Each scanning cycle takes 1 s, providing a temporal data resolution of about 1 s.

Apart from the patterns mentioned above, a horizontal scanning line perpendicular to the bridge deck, starting at ca. 5 m and ending at ca. 105 m from the deck, was also monitored. The data analysis for this pattern is not reported in this paper but an analysis of the 2D wind along a perpendicular line for the same bridge has previously been reported (Nafisifard et al., 2021).

### 2.4. Events studied

The campaign was running for approximately three months, starting August 6th and ending November 2nd. During the period mentioned, lidars were recording the wind field according to the designated scanning line as explained in subsection 2.3.1. Since the quality of the data measured by lidars depends on many parameters e.g. the amount of particles present in the air, the direction of the wind with respect to the laser steering beam, etc., a quality control investigation was first considered to select the periods of sufficient quality. In Table 2, five events, together with their associated patterns and purpose of selection, are reported as measurement cases studied. Moreover, the mean horizontal wind speed, mean wind direction and temperature based on the anemometry recordings are included. Wind direction has been calculated with respect to the bridge axis, which itself has a  $42^\circ$  deviation from the geographic North, as indicated in Fig. 1c.

## 3. Analysis methods

### 3.1. LOS velocity estimation

The Doppler spectra in this experiment are stored in 512 bins, each with a resolution of ca. 234 kHz or alternatively,  $0.183 \text{ ms}^{-1}$ . The following step-wise velocity estimation procedure is applied to the recorded data to flag radial velocity with a low signal-to-noise ratio:

1. The lidar Doppler spectra are set to their original magnitude by applying a scaling factor since the spectra are scaled in order to make best use of the 16 bits used for storage.
2. “Wind-free background spectra” are estimated individually for each lidar. These spectra are dependent on the lidars and not on the air flow being observed.
3. The recorded lidar Doppler spectra are flattened by dividing them with the spectra obtained in step 2.

**Table 1**

Properties of the Doppler wind lidar short-range WindScanner system installation.

Properties	Values
Wavelength	1.565 $\mu\text{m}$
Shortest range	approx. 10 m
Longest range	approx. 200 m
LOS sampling frequency	322 Hz
Lidars' LOS detection range	$-46.8 \text{ m.s}^{-1}$ to $+46.8 \text{ m.s}^{-1}$

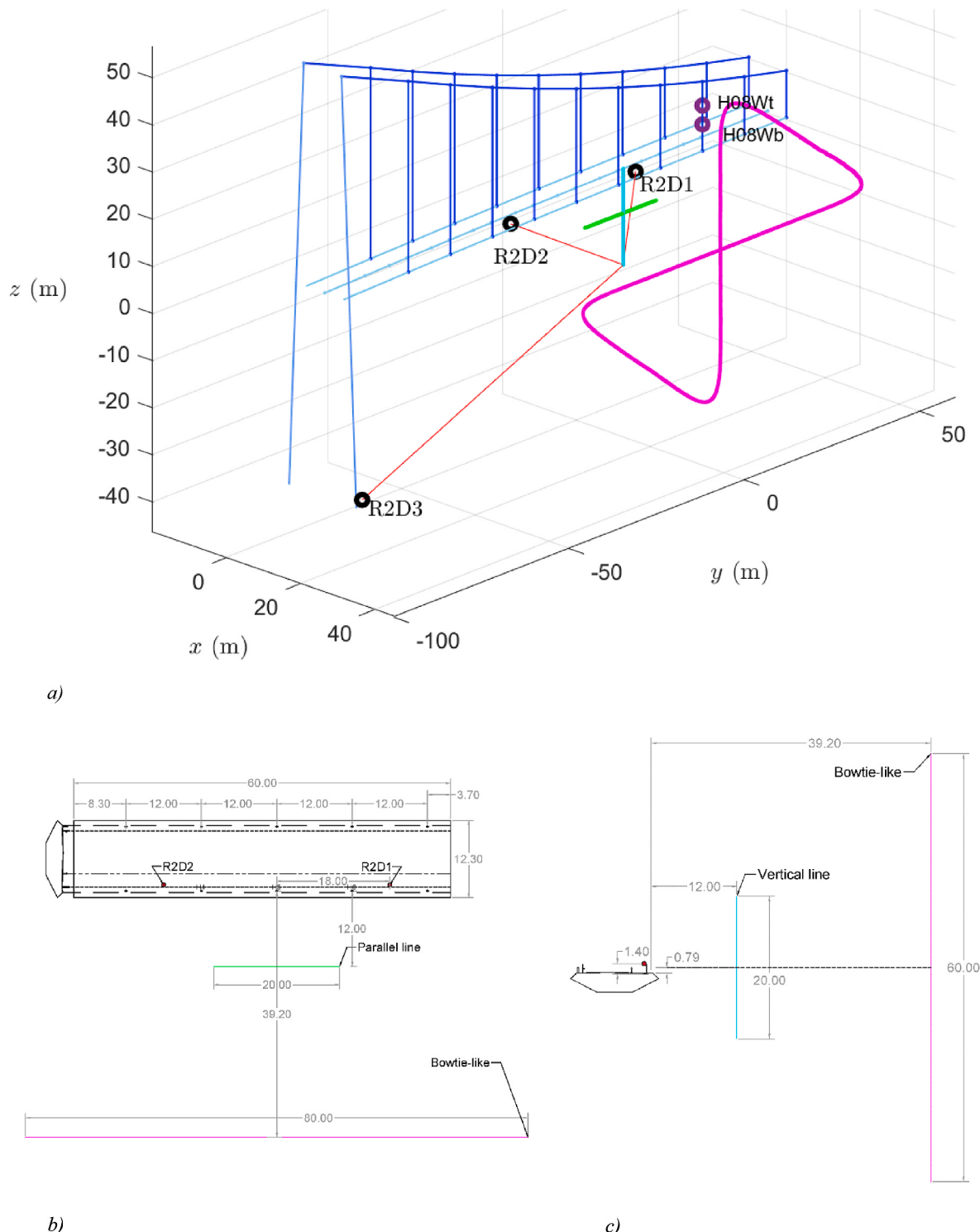


**Fig. 4.** Lidar measurement setup. a) The triple-lidar measurement setup. b) Top view of the measurement domain. c) Side view of the measurement domain.

4. The flattened spectra are filtered by applying a threshold at the level of the mean plus  $m$  times the standard deviation in a wind-free range, i.e., the 50 frequency bins at the end of each spectrum (see Section 3.2).
5. LOS velocities are estimated based on the median frequency estimator, and the results are compared with those based on two other common methods, namely, the maximum frequency estimator and the centroid frequency estimator.
6. To remove outliers, a Hampel filtering with a window length defined by 20 neighbouring samples on both sides of each sample and three standard deviations away from the local median was applied on the time series of LOS velocities derived by the median frequency estimator (Pearson, 2005).

### 3.2. Threshold estimation

As mentioned in step 4 of section 3.1, it is of great importance to

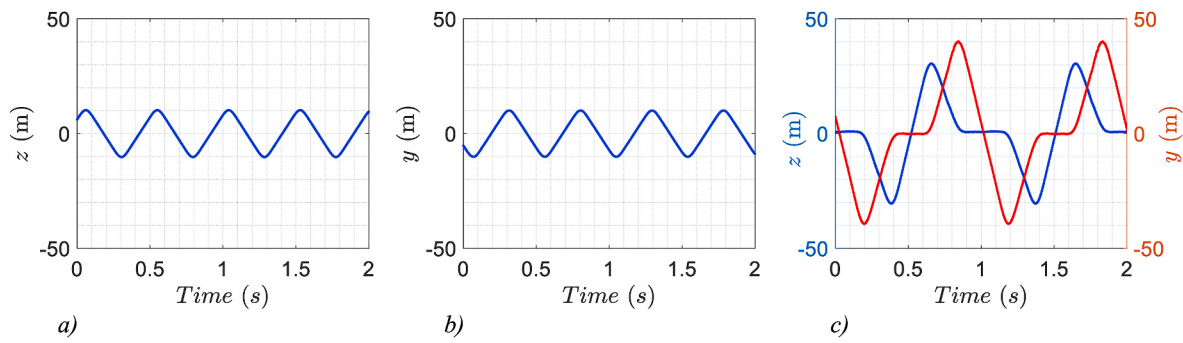


**Fig. 5.** Positions of the lidars scanning volumes along the scanning lines. a) Vertical line. b) Parallel line. c) Bowtie-like.

**Table 2**  
Measurement cases studied.

Date and Time	Name	Pattern	Flow Direction	Purpose	Mean horizontal wind speed ( $\text{m.s}^{-1}$ )	Mean wind direction <sup>a</sup> (°)	Temperature (°C)
23/09/2021 10:23–10:33	I1	Vertical line	S-SW	Validation	6.07	250	11.5
13/10/2021 15:34–15:44	W1	Vertical line	N-NE	Wake analysis	5.23	56	12.8
13/10/2021 15:54–16:23	W2	BowTie	N-NE	Wake analysis	5.74	53	12.8
22/09/2021 01:08–01:18	W3	Parallel line	N-NE	Wake analysis	6.87	58	12.1
22/09/2021 02:56–03:09	W4	Vertical line	N-NE	Wake analysis	5.0	63.5	12.5

<sup>a</sup> Direction relative to bridge axis, equal to direction measured from North plus 42°.

determine the optimum threshold level to remove the spectral noise fluctuations. Commonly, the threshold level is defined as the mean plus  $m$  times the standard deviation in a wind-free range, e.g., the 50 bins (for this study) at the end of each spectrum. Therefore, the  $m$  is a key parameter in defining the threshold. Attempts are made to identify the optimum value of  $m$ , by displaying the mean of absolute difference (MAD) between consecutive values of the LOS velocity derived from the median frequency estimator (Angelou et al., 2012a) as well as the percentage of NaNs (not a number “values”) in the calculated LOS velocity versus the  $m$  (Fig. 6). NaN has been assigned to a sample as the calculated LOS when the estimator is not able to flag the LOS velocity in the filtered flattened spectra due to, e.g. the low concentration of aerosols in the air, flow perpendicular to the laser beam orientation, etc. The value for  $m$  has been incremented in steps of 0.1 from 0 to 7 for each of the three lidars separately.

In Fig. 6, variation of mean absolute differences and percentage of NaNs versus the different number of  $m$  are displayed for the data recorded during event W1. Accordingly,  $m$  equal five is considered to be an appropriate choice for further lidar data analysis as it is associated with the least MAD and reasonable percentage of NaNs, especially with

respect to R2D1. For other events studied, more or less, the same results, as indicated in Fig. 6, are seen, which makes the  $m$  of 5 a constant value for tuning the level of the threshold for all lidars.

### 3.3. Data clustering and synchronisation

A clustering approach was applied to the data in order to acquire more reliable LOS velocities from the lidar recordings in the vertical and parallel scanning patterns. The measurement lines are divided into segments half a meter in length, and all the consecutive spectra within each segment are averaged. The sample time is taken as a direct average of all individual sampling times in the segment, while the LOS velocity is derived from the averaged spectrum of the data samples following the steps explained in 3.1. Fig. 7 illustrates a cluster where ten samples are represented by a single value computed from the averaged spectrum. Besides, sonic recordings are projected onto the laser beam orientation. It can be deducted from Fig. 7 that the data clustering approach provides an enhanced reliability of the LOS speeds, especially when the Doppler spectra within a cluster are more scattered in terms of the LOS velocities they are providing.

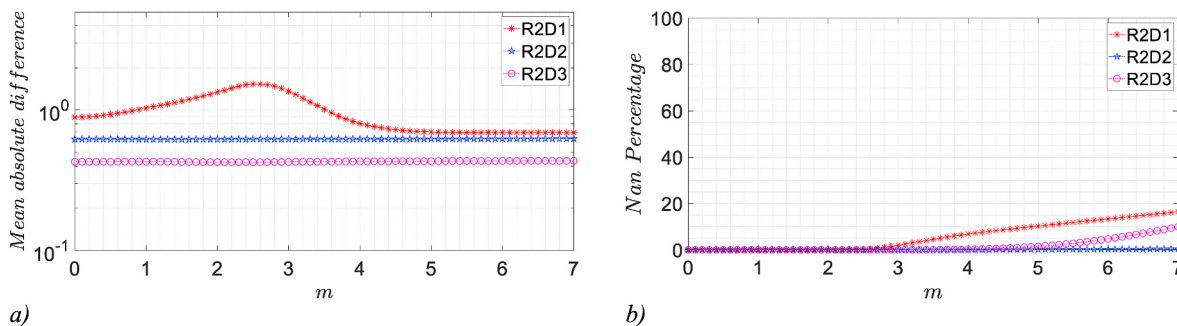


**Fig. 6.** Threshold estimation (case W1 from Table 2: disturbed flow recorded on 13 October 2021, from 15:34 to 15:43). a) MAD vs spectra threshold level. b) NaN percentage vs spectra threshold level.

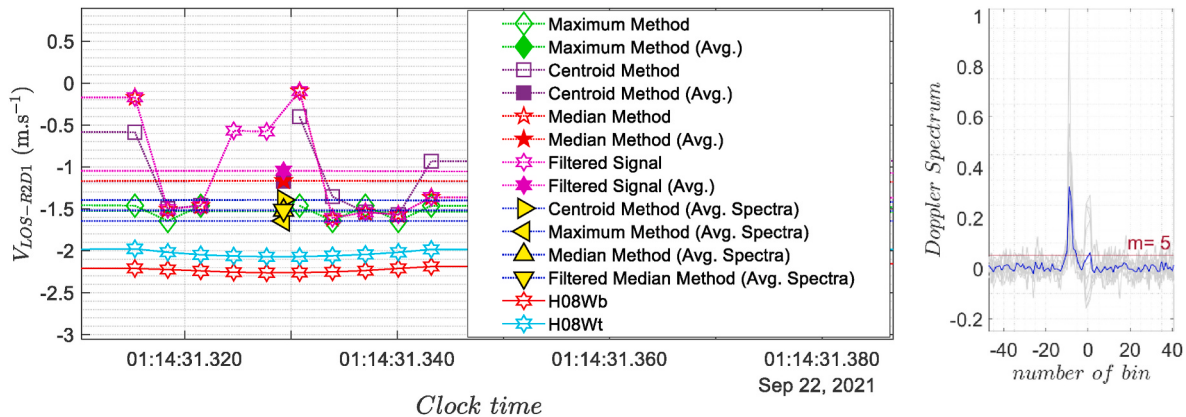


**Fig. 7.** Example of one cluster (left) and associated averaged Doppler spectra (right). The threshold of the averaged spectrum is illustrated by the dark red solid line in front of the individual spectra of the cluster chosen (in grey).

Non-uniform sampling frequency in the vertical and the parallel scanning patterns needs to be addressed when computing the cross-spectra and the cross-correlation. Two approaches were considered to create data with a uniform sampling period. The first approach was to group the data into two families, one for increasing and the second one for decreasing coordinate values along the scanning line, i.e. one for each of the two scanning directions. Within each family, for each segment along the scanning line, a fixed time step of 1 s is obtained in this manner, but a time lag between the sampling times in different segments along the line remains. The spectral estimates obtained for the two families are averaged, and the result is corrected in the frequency domain for the phase lag associated with the non-synchronous samples. The second approach was to use linear interpolation so that the data is resampled at a sampling frequency equal to the maximum sampling frequency of the scanning pattern being observed. This happens for all the segments within the scanning pattern except for two ends of the line, which have equal but half with respect to all other segments. The first would result in a sampling frequency of 2 Hz for all the segments along the scanning line, but the latter provides a sampling frequency of 4 Hz. In this study, the latter approach is implemented, while the former is used for validation.

### 3.4. Wind components retrieved

By using the three LOS velocities derived from the median frequency estimator for each cluster and filtered by the Hampel method, it is possible to extract the 3D wind components in any desired direction using a geometrical transformation, provided that the determinant of the three LOS unit vectors at each measurement position is “sufficiently” different from zero, i.e., that the three light beams are not coplanar (Fuertes et al., 2014; Mann et al., 2009). To do so, first, the azimuth and elevation angles,  $\alpha$  and  $\beta$  respectively, for each lidar are calculated:

$$\alpha_n = \arctan\left(\frac{x_{sp} - x_n}{y_{sp} - y_n}\right) \quad (1)$$

$$\beta_n = \arcsin\left(\frac{z_{sp} - z_n}{\sqrt{(y_{sp} - y_n)^2 + (z_{sp} - z_n)^2}}\right) \quad (2)$$

The staring point (denoted by subscript sp) is the common steerable measurement “point” at all times, and  $n$  identifies the lidar unit ( $n = 1, 2, 3$ ). The measured LOS velocities have a relation with the perpendicular wind components as follows (Fig. 8).

$$\overrightarrow{OP} = (x_{sp} - x_n, y_{sp} - y_n, z_{sp} - z_n) = (R \cos(\beta)\sin(\alpha), R \cos(\beta)\cos(\alpha), R \sin(\beta)) \quad (3)$$

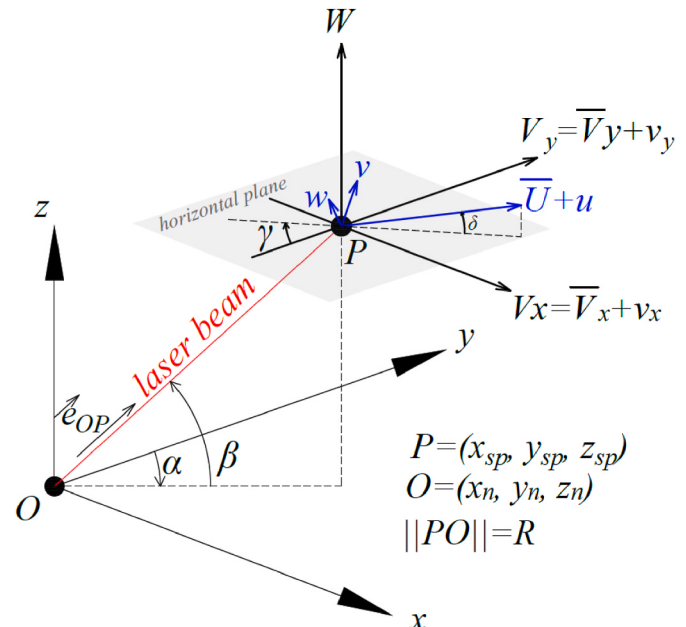


**Fig. 8.** Measurement of the radial wind speed and wind-based coordinate system.

$$\begin{aligned} \vec{e}_{OP} &= \frac{\overrightarrow{OP}}{\|\overrightarrow{OP}\|} = \frac{\overrightarrow{OP}}{R} = \frac{(R \cos(\beta)\sin(\alpha), R \cos(\beta)\cos(\alpha), R \sin(\beta))}{R} \\ &= (\cos(\beta)\sin(\alpha), \cos(\beta)\cos(\alpha), \sin(\beta)) \end{aligned} \quad (4)$$

$$\begin{aligned} V_{LOS_n} &= \vec{V} \cdot \vec{e}_{OP} = (V_x, V_y, V) \cdot (\sin(\alpha)\cos(\beta), \cos(\alpha)\cos(\beta), \sin(\beta)) \\ &= V_x \cdot \sin(\alpha)\cos(\beta) + V_y \cdot \cos(\alpha)\cos(\beta) + V \cdot \sin(\beta) \end{aligned} \quad (5)$$

Having established the relation between LOS velocities and the wind components, the wind components, normal and parallel to the deck, which are denoted by  $V_x$  and  $V_y$ , and vertical component denoted by  $V$  could be obtained by rewriting the equation above for all three LOS velocities in matrix form as:

$$[V_{LOS1} \quad V_{LOS2} \quad V_{LOS3}] \mathbf{M}^{-1} = [V_x \quad V_y \quad V] \quad (6)$$

where  $\mathbf{M}$  is defined as

$$\mathbf{M} = \begin{bmatrix} \sin(\alpha_1)\cos(\beta_1) & \sin(\alpha_2)\cos(\beta_2) & \sin(\alpha_3)\cos(\beta_3) \\ \cos(\alpha_1)\cos(\beta_1) & \cos(\alpha_2)\cos(\beta_2) & \cos(\alpha_3)\cos(\beta_3) \\ \sin(\beta_1) & \sin(\beta_2) & \sin(\beta_3) \end{bmatrix} \quad (7)$$

In this formulation, the angle between the main wind direction and the bridge axis, also called the yaw angle, is:

$$\gamma = \arctan \left( \frac{\bar{V}_x}{\bar{V}_y} \right) \quad (8)$$

where  $\bar{V}_x$ , and  $\bar{V}_y$  are the average of across-deck and along-deck wind components at each separate height. The wind-based coordinate system is illustrated in Fig. 8. Besides, the inclination angle, which is the angle of the wind direction and the horizontal plane, is defined by  $\delta$  as:

$$\delta = \arctan \left( \frac{\bar{W}}{\sqrt{\bar{V}_x^2 + \bar{V}_y^2}} \right) \quad (9)$$

In which,  $\bar{W}$  is the average of vertical wind components for each altitude. Finally, the calculated wind components  $V_x$ ,  $V_y$ , and  $W$  are aligned with the main wind direction to obtain the along-wind ( $\bar{U} + u$ ) as well as zero-mean across-wind ( $v$ ) and vertical wind fluctuations ( $w$ ).

### 3.5. The lidar data resolution

Doppler wind lidars measure wind velocity in a volume stretched along the beam. The full width at half maximum (FWHM) expresses the spatial resolution of the volume being measured by a continuous-wave lidar (Mikkelsen, 2009), and it increases quadratically with the distance from the point where the light is focused (as shown in equation (10)).

$$Z_R = \frac{\lambda r^2}{\pi a_0^2} \quad (10)$$

Here  $\lambda = 1.565 \mu\text{m}$  is the wavelength of the laser source;  $r$  is the focus distance, and  $a_0$  is the effective beam radius, which in ideal condition is ca. 28 mm. Table 3 presents the range of FWHM along the different scanning lines for three lines. In general, the longer the distance from the lidars to the steering point, the larger the volumes being observed. Accordingly, ground lidar (R2D3) measures the along-beam velocity within larger volumes due to its larger distance to the lines being measured compared to deck lidars. Deck lidars also capture the LOS velocity with identical FWHMs, except for the vertical line pattern, in which they show slight differences due to the curved geometry of the bridge deck.

### 3.6. Error propagation in lidar data retrieved

In Eq. (6), the inverse of matrix  $\mathbf{M}$  is required to solve the system of linear equations and obtain the velocity components perpendicular to and along the bridge deck. However, the accuracy of the results depends on the condition number of the matrix  $\mathbf{M}$  which reflects to what degree the vectors formed by the three lidar beams are linearly independent, i.e. to what degree the three lidar beams capture all the different directions in space. The condition number is a mathematical tool revealing the sensitivity of the solutions to the changes in the input matrix (Chapra and Canale, 2010). The 2-norm condition number of matrix  $\mathbf{M}$  is defined

**Table 3**

The range of full width at half maximum (FWHM) for all scanning patterns studied.

	Vertical line		Parallel line		BowTie	
	FWHM (m)		FWHM (m)		FWHM (m)	
	max	min	max	min	max	min
R2D1	0.72	0.58	1.17	0.28	5.47	2.36
R2D2	0.78	0.64	1.17	0.28	5.47	2.36
R2D3	9.6	7.6	10.32	6.75	17.25	4.73

as

$$\text{Cond} [\mathbf{M}] = \|\mathbf{M}\| \|\mathbf{M}^{-1}\| \quad (11)$$

where the  $\|\mathbf{M}\|$  and  $\|\mathbf{M}^{-1}\|$  are the norm of matrix  $\mathbf{M}$  and matrix  $\mathbf{M}^{-1}$  (the inverse of  $\mathbf{M}$ ). If the equation system is ill-conditioned, the condition number is considerably greater than unity, and the transformation of the wind velocity components is unreliable, which results in a larger uncertainty in the obtained wind velocity components.

The variation of the condition number along the scanning line for the three scanning patterns introduced is shown in Fig. 9. Depending on the pattern, the largest condition numbers are seen at the end of the scanning lines toward the south or the sea surface. However, the values are relatively small and the adopted measurement configurations are well-suited for reliable estimation of the three wind velocity components.

### 3.7. Single and two-point statistics

#### 3.7.1. Spectral analysis

Welch's spectral estimator based on averaged results for overlapping segments (Welch, 1967) is used to calculate the spectra of the wind velocity components, which are then bin averaged along a logarithmic abscissa. A 10-min wind data is analysed and divided into segments of 5 min with 50 % overlapping (Carter et al., 1973). In contrast to sonic anemometers, which monitor flow in a point-like volume, as mentioned earlier, Doppler wind lidars measure wind velocity in a volume stretched along the beam, in which the high-frequency components of the wind are consequently "smoothed" out. A comparison of an along-beam wind velocity spectrum with a corresponding wind spectrum from a sonic anemometer will show an attenuation of the spectrum at higher frequencies (Sjöholm et al., 2009; Angelou et al., 2012b).

#### 3.7.2. Coherence

Coherence is a frequency-dependent correlation of wind velocity fluctuations, defined as the normalized cross-spectral density of wind components  $S_{ij}$ , simultaneously measured in two points,  $i$  and  $j$ , with a spatial separation  $d = l_i - l_j$ . The so-called co-coherence captures the in-phase variation of the velocity components at different frequencies:

$$CCoh_{ij}(f) = \frac{\text{Re}(S_{ij}(f))}{\sqrt{S_i(f) \cdot S_j(f)}} \quad (12)$$

where  $S_i$  and  $S_j$  are the auto spectral density of wind components. Accordingly, the quad-coherence can be expressed as (Davenport, 1961):

$$QCoh_{ij}(f) = \frac{\text{Im}(S_{ij}(f))}{\sqrt{S_i(f) \cdot S_j(f)}} \quad (13)$$

#### 3.7.3. Cross-correlation coefficient

The cross-correlation coefficient between any desired fluctuation components (Called  $v_i$  and  $v_j$ ), simultaneously measured at two separated points,  $i$  and  $j$  with spatial separation  $d = l_i - l_j$  is also of importance. This nondimensional quantity is defined as:

$$\rho_{v_i v_j} = \frac{E[v_i v_j]}{\sigma_{v_i} \sigma_{v_j}} \quad (14)$$

Where  $\sigma$  and  $E$  are the standard deviation and the cross-covariance function operators, respectively.

### 3.8. Drag coefficient

Considering the conservation of momentum, the drag force coefficient can be calculated by evaluating the velocity deficit in the wake as below:

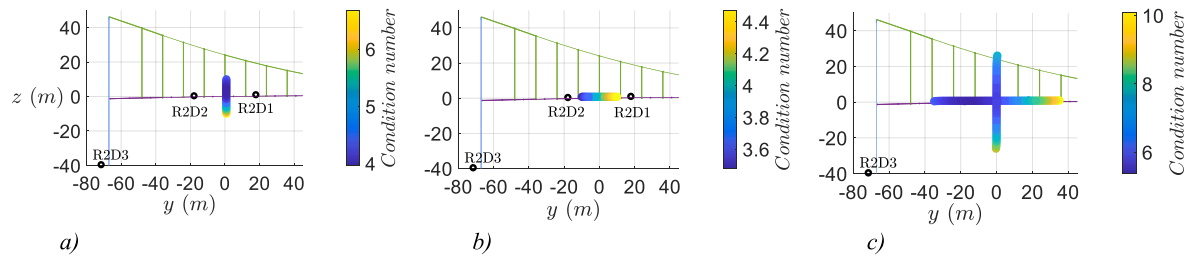


**Fig. 9.** Condition number along the scanning line. a) Vertical line. b) Parallel line. c) Bowtie-like.

$$C_d = \frac{2}{H\bar{U}^2} \cdot \int_{z_1}^{z_2} \bar{U}(z) \cdot [\bar{U} - \bar{U}(z)] dz \quad (15)$$

where  $H = 2.76$  m is the deck height,  $\bar{U}$  is the mean undisturbed along-wind speed evaluated at  $z_1$  and  $z_2$ , and  $\bar{U}(z)$  is the mean wind speed within the wake area.

#### 4. Measurement results and discussions

##### 4.1. Validation

Data recorded on September 23rd is used to illustrate the validation of the lidar measurements against the sonic anemometer data. The 10-min-long event starting from 10:23 is characterised by a wind direction of  $250^\circ$ , i.e., the flow moving from outside of the fjord towards the bridge. The wind velocities observed ca. 11 m upstream from the bridge deck are considered undisturbed by the bridge, as well as the anemometer data recorded on the upstream side of the deck. The mean wind speed, mean wind direction and temperature are given in Table 2. The lidars were scanning the flow along a vertical line 11 m from the bridge deck, as explained in Section 2.3.1. The time series of the horizontal wind velocities across ( $x$ ) and along ( $y$ ) the deck, as well as the vertical component, are displayed in Fig. 10, recorded at roughly 10 m above the deck by the lidars and a sonic anemometer (H08 wt). Generally, the velocity components recorded by the WindScanners agree

well with those obtained by the sonic anemometer. The minor discrepancies observed between the lidar and sonic data can be attributed to the fact that the observed locations in space are not identical and have a lateral separation of ca. 37 m in the horizontal plane.

A good agreement between the lidar and the sonic data is also found in terms of their spectral contents, as illustrated in Fig. 11. The power spectral densities of the WindScanners are obtained by averaging spectra for all levels along the scanning line, with a grid size of 0.5 m. The small sampling volume of deck and ground lidars ensures representative spectral content at higher frequencies. As in section 4, bridge deck height  $H$  is adopted as a reference length.

##### 4.2. Wind characteristics

The capability of lidars in measuring the wind field with the high spatiotemporal resolution is illustrated in Fig. 12, in terms of the along-wind component as well as across-wind and vertical wind turbulences, along the vertical line downstream of the bridge deck (W4). In that event, the wake is seen systematically during the 13-min period, especially in terms of a notable reduction of the along-wind component. It is worth mentioning that across-wind and vertical components have zero-mean time series and are of low magnitude, consequently.

Several wind characteristics associated with the data in Fig. 12, are presented in Fig. 13 for a selected height of  $z = -2$  m, which is 0.4 m below the girder trailing edge (Fig. 4c), close to the middle of the

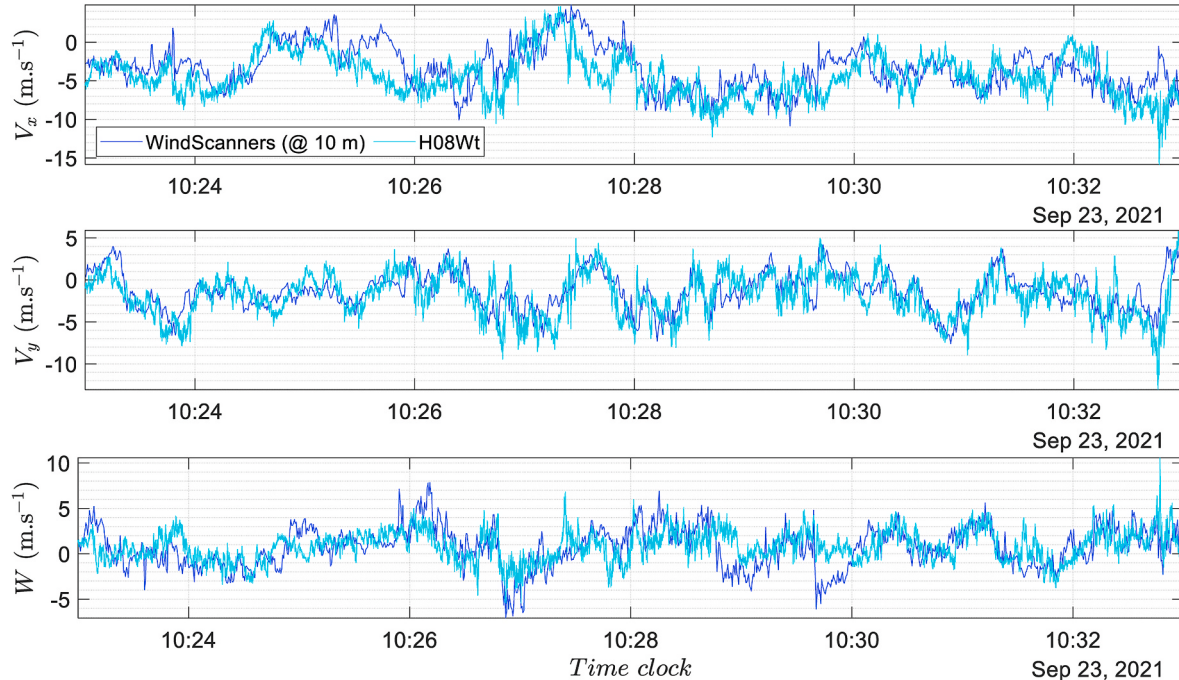


**Fig. 10.** Across-deck, along-deck and vertical wind components recorded by WindScanners along the vertical line and anemometer (H08 wt) (case I1 from Table 2: undisturbed flow recorded on 23 September 2021, from 10:23 to 10:32).

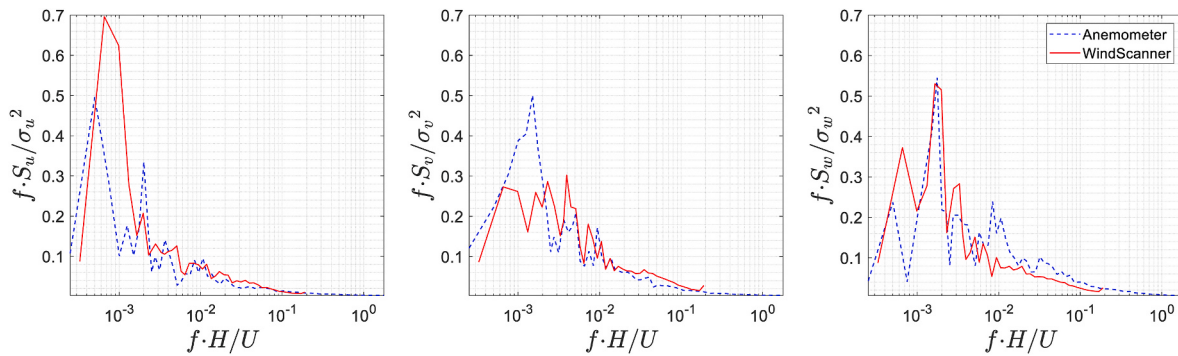


**Fig. 11.** Power spectral density of the along-wind (left) and across-wind components (right) measured by the WindScanners along the vertical line and anemometers (case I1 from Table 2: undisturbed flow recorded on 23 September 2021, from 10:23 to 10:32 along the vertical line).

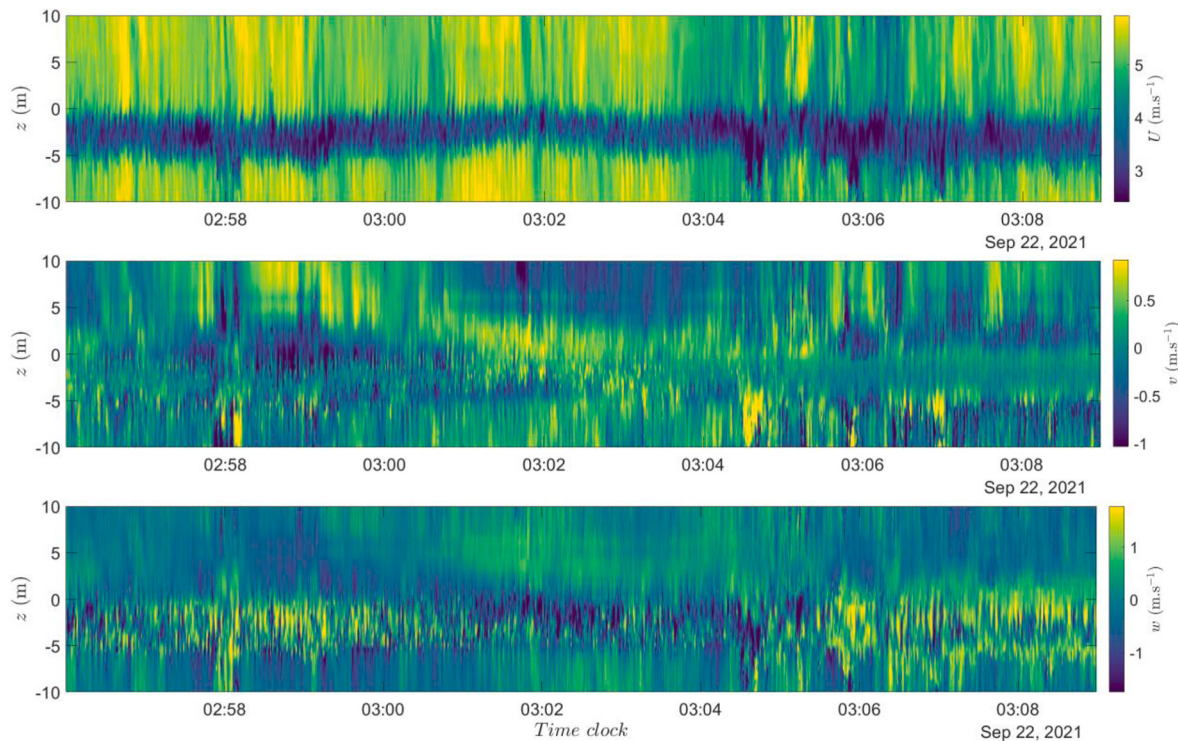


**Fig. 12.** Along-wind (top), across-wind turbulence (middle) and vertical turbulence (bottom) components measured by the WindScanners along the vertical line (case W4 from Table 2: disturbed flow recorded on 22 September 2021, from 02:56 to 03:09).

vertical scanning line. The parameters shown are the wind direction, inclination angle and the three perpendicular velocity components in the bridge coordinate system, both from the WindScanners and the sonic anemometers on hangers 8 and 10. The figure provides a certain insight into the wake and the differences caused by the different spatial locations of the sonic anemometers and the scanning line (see Fig. 4). High-magnitude fluctuations for all quantities mentioned clearly indicate the complex flow regime inside the wake of the bridge deck.

At the top of the vertical scanning line ( $z = 10$  m), where the flow is only affected by the bridge girder to a limited degree, a good agreement is observed between the lidar and the sonic data at hangers 8 and 10, some distance away. While a time-series comparison is not included here, for brevity, the corresponding mean values at  $z = 10$  m are included in the next section, together with the mean values recorded by the sonic anemometers.

#### 4.2.1. Mean flow characteristics

The mean wind characteristics along the vertical line one deck width

downstream of the bridge girder, for cases W1 and W4, are displayed in Fig. 14. The overall profiles are similar for the two cases, as expected since the velocity level and wind direction are similar. In the wake region, the relative velocity deficit of the component parallel to the bridge is smaller than of the one normal to the bridge, making the flow veer towards the bridge axis by about  $10^\circ$  and  $7^\circ$  at the wake center, in the W1 and W4 cases, respectively. In both of the “near wake” observations (W1 and W4) an increase in the angle of attack is observed at the wake center, compared to the free flow. This is most likely due to an asymmetry of the bridge girder cross-section, with the trailing edge located closer to the upper than to the lower deck surface, partly directing the flow upwards.

One distinct feature of the W1 case is the large negative inclination angles derived from the lidar data (in the order of  $-10^\circ$ ) along the entire scanning line. Case W4 has a smaller, although still slightly negative, inclination angle along the vertical line in the undisturbed zone and shows a more consistent similarity with the measurements from the sonic anemometers. This difference between the parameters defined

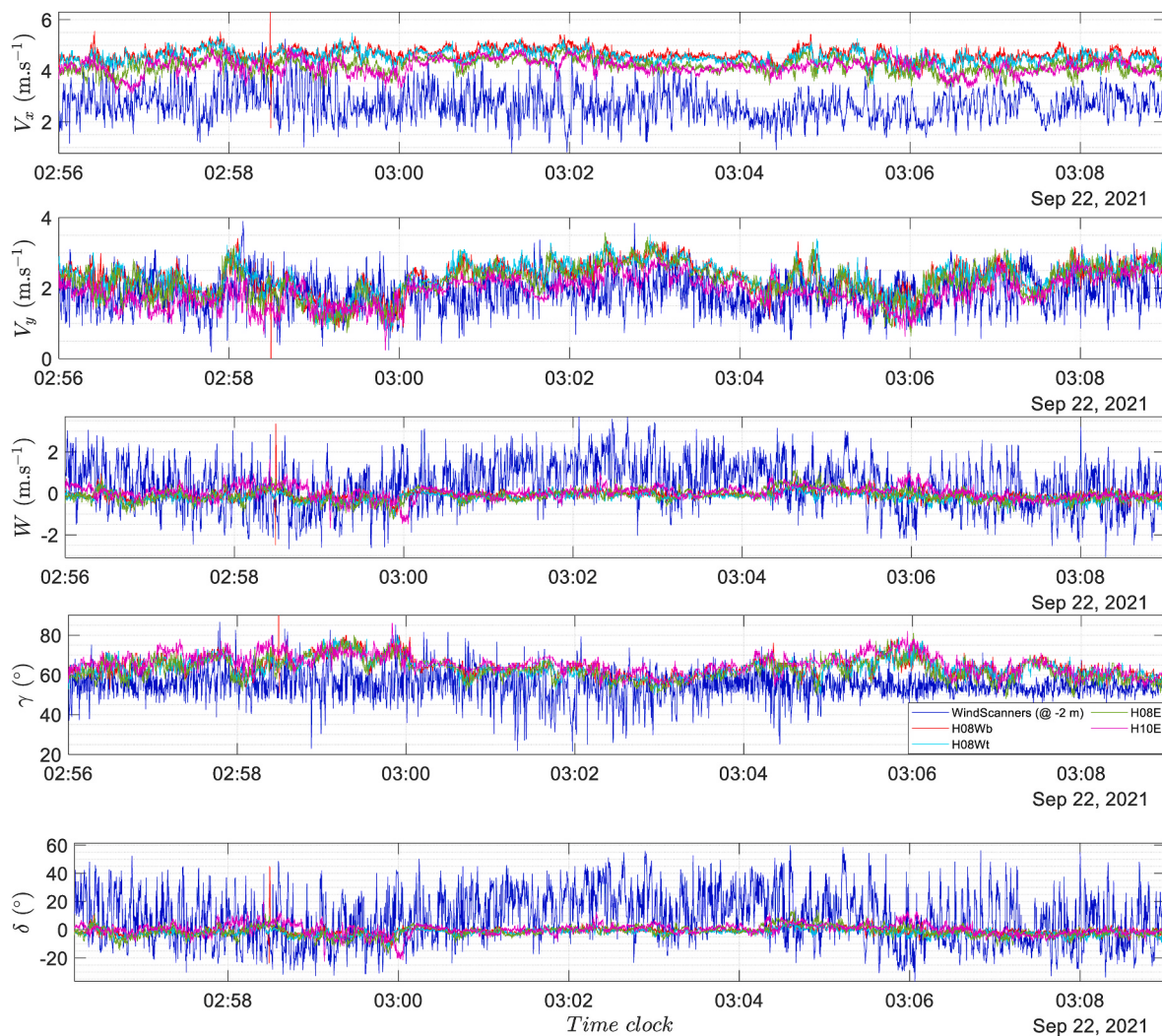


**Fig. 13.** Time-series of across-deck, along-deck, and vertical velocity component, wind direction and inclination angle (from top to bottom), measured by the WindScanners in the wake at  $z = -2$  m on the vertical line, compared to simultaneous measurements by sonic anemometers at hangers 8 and 10 (case W4 from Table 2: recorded on 22 September 2021, from 02:56 to 03:09).

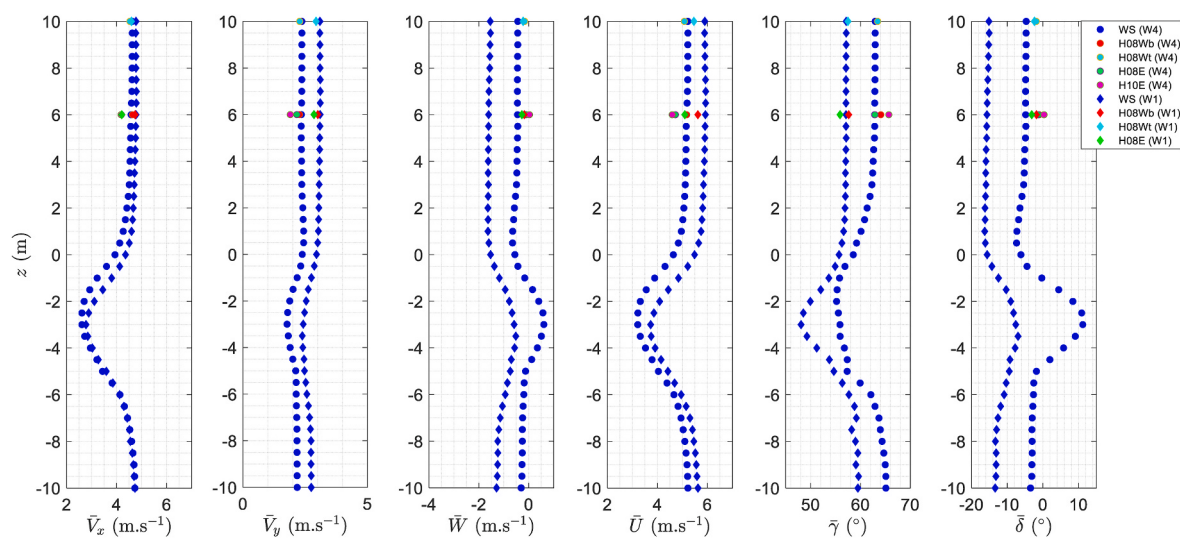


**Fig. 14.** Wind profiles of across-deck, along-deck, and vertical component, along-wind component, wind direction, inclination angle (from left to right), measured by the WindScanners along the vertical line compared to simultaneous measurements by anemometers (case W1 and W4 from Table 2: disturbed flow recorded on 13 October 2021, from 15:34 to 15:43, and 22 September 2021, from 02:56 to 03:09).

within the vertical plane for case W1 and W4, implies that these flow parameters are sensitive to the flow conditions. The fact that in case W1 the WindScanners show different vertical velocity and inclination angle than the sonic data in the undisturbed zone, is not fully understood, but may be related to a wind descending from the mountains N-NE of the bridge, with a larger downward component at the scanning line position compared to that of the sonic anemometer further south. In the case of undisturbed flow from S-SW (I1), the flow inclinations captured by the sonic and the lidars were consistent (see Fig. 10), as well as for case W4. This and the overall similarities in the fluctuations of the vertical turbulence captured by both types of instruments suggest that the negative inclination seen in Fig. 14 for case W1 is likely due to local terrain effects for that wind direction.

To further study the negative significant flow inclination observed for Case W1, 11 m from the deck trailing edge (Fig. 14), a second mean wind velocity profile is estimated 28 m further downstream, using the BowTie scan data recorded 20 min later. The two mean velocity profiles are compared in Fig. 15. A downward shift of the position of the wake center can be observed in the wind profile further downstream. This provides an additional way of assessing the inclination angle since the horizontal distance between two patterns ( $\Delta y$ ) and the shift of the wake center in the vertical direction ( $\Delta z$ ) are known. Two patterns are located 11 m and 39 m downstream from the bridge trailing edge. Accordingly,  $\delta = \text{atan} \left( \frac{\Delta z}{\Delta y} \right) = \text{atan} \left( \frac{5.5 \text{ m}}{-28 \text{ m}} \right) = -11^\circ$  which is consistent with the range of angles of attack derived from the lidar data, as presented in Fig. 14. This reinforces the understanding that the negative inclination angle derived from the lidar data around hanger 5 reflects the local flow phenomenon associated with the wind from N-NE and a rather limited mean wind speed ( $\bar{U} = 5.9 \text{ m.s}^{-1}$ ).

The lidars also scanned the flow velocity components along a parallel line, with the length of 20 m, centred in front of hanger 5 and around one deck width ( $LB = 12.3 \text{ m}$ ) from the deck in the wake, as listed in Table 2 (W3). Fig. 16 shows the mean flow orientation and velocities along the scanning line. The negative inclination angle with a magnitude similar to the one observed for case W1 is noteworthy. It is accompanied by a downward vertical wind component. A slight change in wind direction and inclination angle towards the middle of the bridge is also noticeable which is likely due to the curved deck and the fact that toward the middle of the bridge span the vertical distance between the scanning line and the deck surface is reduced. The wind velocity components, on the

other hand, are relatively constant along the scanning line. The angle of attack is seen to be sensitive to minor variation of the mean vertical wind speed, combined with the relatively low incoming wind speed.

#### 4.2.2. Drag coefficient

From the mean velocity profile in the wake, the drag coefficient of the bridge deck, formed as a hexagonal closed box, can be estimated using the method explained in section 3.8. In this regard, the boundaries of the wake region need to be defined as the first step. Fig. 15 displays the vertical profiles of the along-wind velocity component. The wake region was defined by  $z_1 = +4 \text{ m}$  and  $z_2 = -10 \text{ m}$  for the vertical scanning line of case W1. In the present case, the drag coefficient is estimated to be  $C_d = 0.91$ . The value is comparable to 0.85, a result obtained in a wind tunnel study, with a section model in cross-flow at  $-10^\circ$  (Hansen, 2021).

#### 4.2.3. Turbulence intensities

Fig. 17 shows the variation in turbulence intensities along the scanning line for three different scanning patterns studied (W1, W3, and W4). For the vertical scanning line, the along-wind turbulence intensities exceed 20% in the wake, for both case W1 and W4, which is double the turbulence level of the undisturbed flow. Whereas case W1 shows more turbulent flow than case W4 for the across-wind turbulence intensities in the wake. A quadruple increase is seen for the vertical turbulence in the wake, compared to the ca. 10% turbulence intensity of the undisturbed flow. The difference in the profiles of the vertical turbulence intensity in cases W4 and W1 is consistent with the different angles of attack of the incoming flow in the two cases: A smaller negative angle of attack in case W4, compared to W1, is associated with a more narrow and elevated wake region. The turbulence intensities along the parallel scanning line show less variation since most of the line is influenced by the bridge deck in a similar manner, except at the southern part of the line towards the middle of the bridge span. For that southernmost region of the scanning line, turbulence intensities for along-wind, across-wind, and vertical turbulences increase and reach up to 11%, 14%, and 16%, for the  $u$ -,  $v$ - and  $w$ -components, respectively, clearly showing an increased interaction between the deck and the incoming flow.

### 4.3. Turbulence characteristics

#### 4.3.1. Wind spectra

The frequency content of turbulence within and outside of the wake (W1) is presented in Fig. 18. The wake flow is represented by six observation points at the central part of the wake, while the four highest-level observation points are selected to study the spectral contents of the undisturbed flow outside the wake. Inside the wake, the spectral peak has a higher frequency (smaller scale turbulence) compared to that of the undisturbed flow, which indicates a flow-deck interaction. The spectrum is centred at a Strouhal number,  $St = f \cdot H / U$ , between 0.1 and 0.2. In other full-scale studies,  $St$  values from 0.15 to 0.25 have been observed, for turbulence intensities  $I_u$  ranging from 0.06 to 0.27 (Dantiotti, 2022).

#### 4.3.2. Cross-correlation coefficient

Synchronisation of the measurements, as discussed in 3.3, enabled estimation of the cross-correlation of the velocities in any two points along the scanning patterns. Fig. 19 (top) shows the cross-correlation coefficient of along wind turbulence at different vertical separations along the scanning line (W1). Note that the results are grouped by their locations with respect to the wake (as defined in 3.8), considering both points inside the wake region, both outside the wake region, or one inside and one outside the wake. The correlation for the case when both points are located outside the wake region is seen to follow a traditional pattern of gradually reduced values of correlation for increased separations. This trend is also observed when one point is within the wake

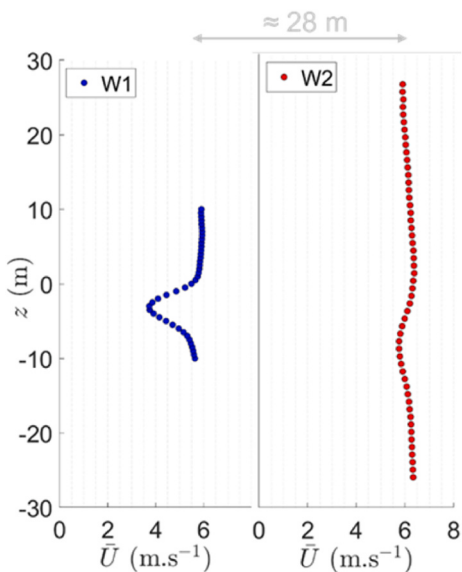


**Fig. 15.** Velocity recorded along a vertical scanning line (case W1) and BowTie scanning pattern (case W2) downstream of the bridge recorded on 13 October 2021.

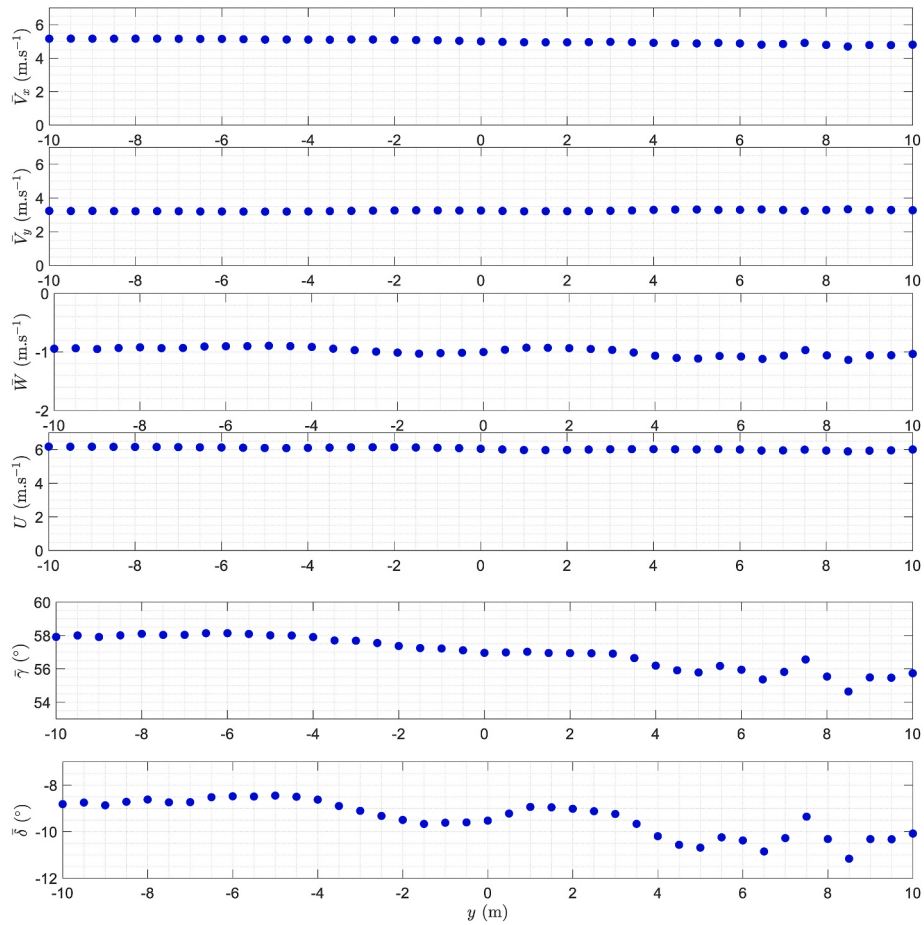


**Fig. 16.** WindScanner observations of across-deck, along-deck, and vertical component, along-wind component, wind direction, and inclination angle (from top to bottom) measured by the WindScanners along the parallel line (case W3 from Table 2: disturbed flow recorded on 22 September 2021, from 01:08 to 01:17).

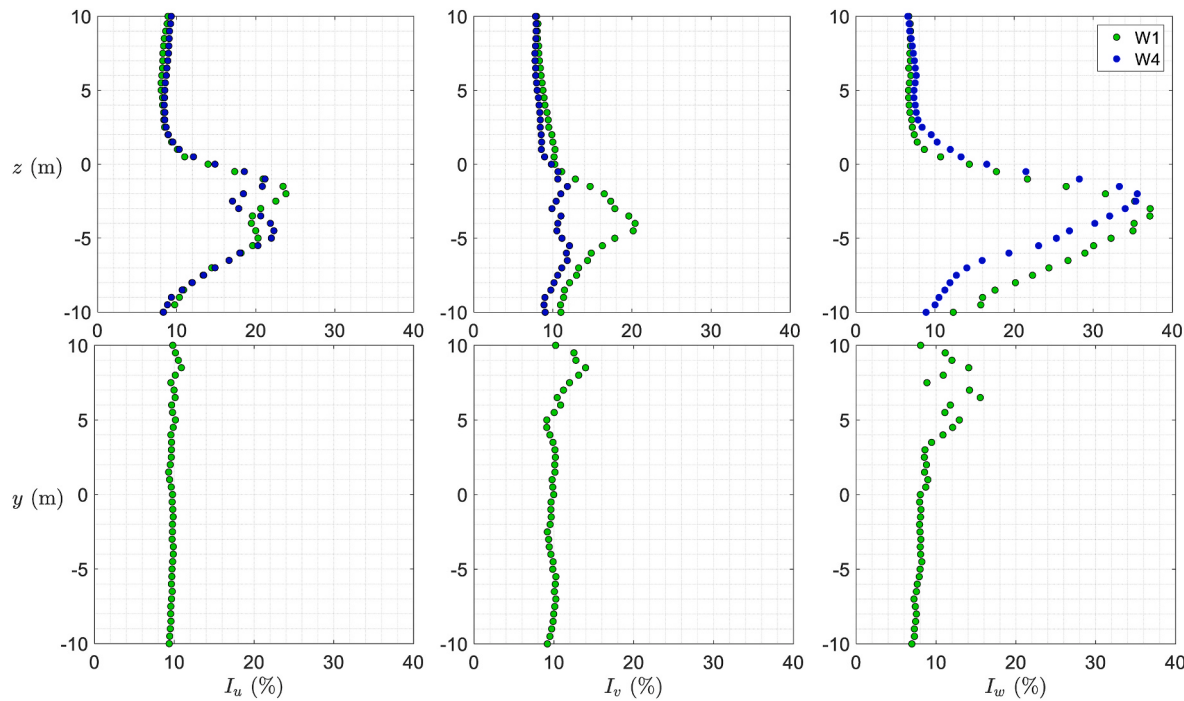


**Fig. 17.** Single-point statistics of atmospheric turbulence measured by WindScanners along the vertical line [case W1 from Table 2: recorded on 13 October 2021, from 15:34 to 15:43; case W4 from Table 2: recorded on 22 September 2021, from 02:56 to 03:09] (top row) and parallel line [case W3 from Table 2 recorded on 22 September 2021, from 01:08 to 01:17] (bottom row).

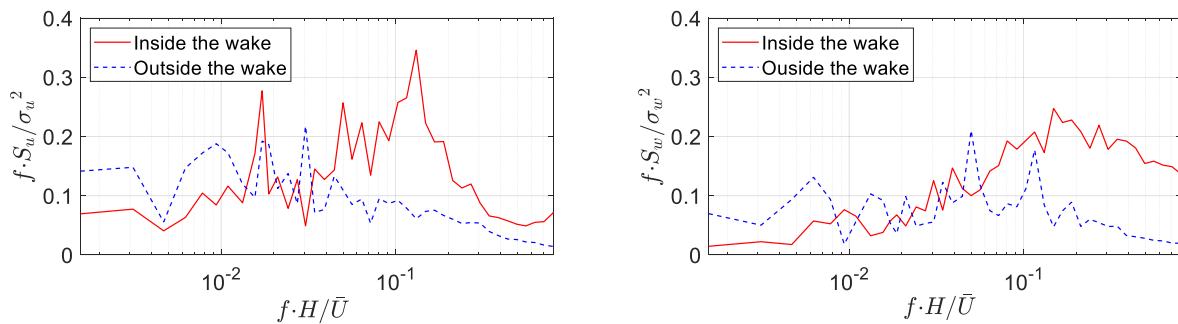


**Fig. 18.** Spectra of along-wind turbulence (left) and vertical turbulence (right) outside and within the wake on the vertical scanning line (case W1 from Table 2: disturbed flow recorded on 13 October 2021, from 15:34 to 15:43).

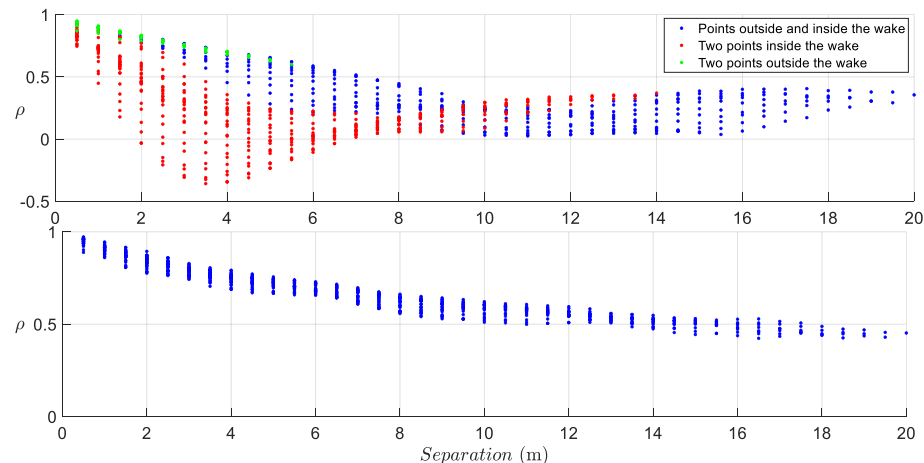


**Fig. 19.** Cross correlation coefficients evaluated based on the WindScanner data, along the vertical line [case W1 from Table 2: disturbed flow recorded on 13 October 2021, from 15:34 to 15:43] (top) and parallel line [case W3 from Table 2: disturbed flow recorded on 22 September 2021, from 01:08 to 01:17] (bottom).

and the other outside. However, when both points are within the wake zone, the correlation becomes strongly negative for certain separations. In Fig. 19 (bottom), the correlation is displayed for horizontal separations covered by the parallel scanning pattern (W3) downstream of the deck, 0.78 m above the roadway. According to the mean velocity profile and the negative inclination angles, the flow at this height is affected by the deck to only a limited degree, and the correlation coefficient decays exponentially, similarly to the lateral correlation of an undisturbed flow.

#### 4.3.3. Coherence

The coherences of along-wind turbulence ( $u$ ) for two pairs of heights, located inside the wake at  $-5$  m and  $-1$  m, corresponding to cross-correlation coefficient of roughly  $-0.4$ , and outside the wake at  $+6$  m and  $+10$  m, with a cross-correlation coefficient of nearly  $0.68$  is shown in Fig. 20. The coherence values are smoothed by applying a moving average function with a window length of 10 data points. They are displayed as a function of frequencies up to 1 Hz, normalized by the ratio of the deck height (2.76 m) and the undisturbed along-wind velocity

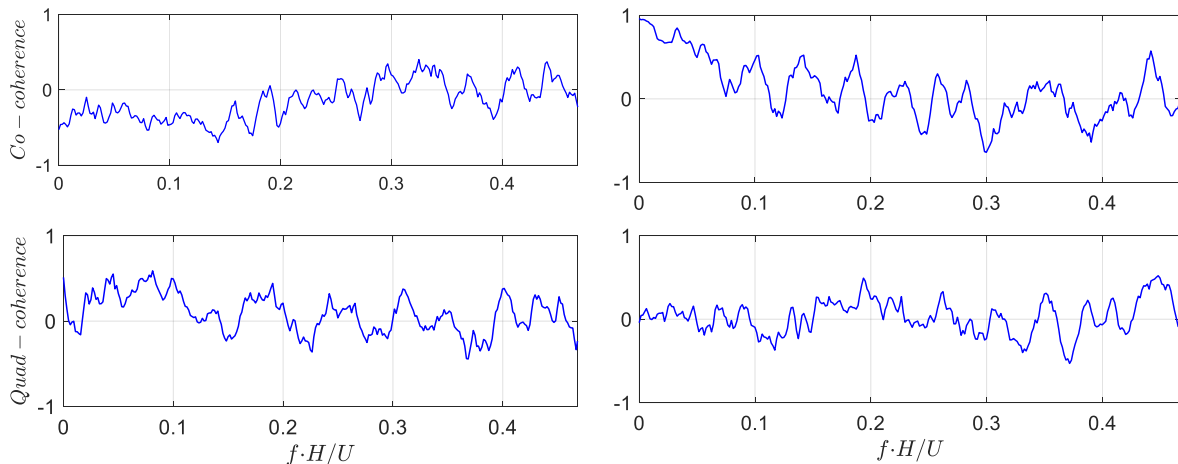


**Fig. 20.** Co-Coherence (top), and Quad-coherence (bottom) inside the wake (left column) and outside the wake (right column), measured by the WindScanners along the vertical scanning line (case W1 from Table 2: disturbed flow recorded on 13 October 2021, from 15:34 to 15:43).

recorded by the WindScanners at the highest altitude of the scanning line.

Negative Co-coherence is seen inside the wake at reduced frequencies up to 0.2, indicating an alternate increase and decrease in the velocities in the upper and lower part of the wake. For relatively undisturbed flow outside the wake, the Co-coherence is positive up to around 0.2. The disturbed and undisturbed regions can also be distinguished by looking at Quad-coherence, which shows positive values for wake-embedded heights up to reduced frequencies of 0.2. The quad-coherence for undisturbed flow fluctuates around zero for low reduced frequencies.

## 5. Conclusions

This paper presents novel triple-lidar measurements of a wind field downstream of a suspension bridge deck, where the wake characteristics along three different scanning lines, two vertical lines at different distances from the deck and one horizontal line, parallel to the deck have been studied. The lidar observations have been verified by comparison with recordings from sonic anemometers above the bridge deck. Conclusions from this study are summarised as follows:

1. The wake can be clearly identified through the along-wind velocity deficit observed along the vertical scanning line.
2. In one of the cases studied, the mean vertical wind velocity was found to be negative along the entire scanning line, thereby reflecting a downward flow. This trend was observed both at 11 m and 39 m downstream of the deck for both the vertical and horizontal scanning lines. This event is believed to reflect how the complex local terrain affects the flow. Regardless of the inclination of the incoming flow, an increase of the angle of attack within the velocity deficit region was identified, likely due to the asymmetry of the bridge girder section.
3. The vertical turbulence intensity along the vertical scanning line is seen to be up to 40% within the wake which is much larger than the ca. 10% turbulence intensity of the vertical velocity in the undisturbed flow. A noteworthy increase is also observed for the two other perpendicular turbulence components.
4. The turbulence intensities along the deck-parallel scanning line show less variation since most of the line is at a similar height relative to the bridge deck, except at the southern part of the line towards the middle of the bridge span, where slightly scattered but increased values are seen, as the scanning line reaches further into the wake.
5. For the yaw angle of 34° from the normal to the bridge axis drag coefficient of 0.91 was derived from the mean wake velocity profile and the associated momentum. The value is comparable to 0.85, a result obtained in a wind tunnel study, with a section model in cross-flow at -10°.
6. The flow-deck interaction was investigated by comparing the velocity spectra evaluated at different altitudes both inside and outside the wake. It was seen that the spectral peak inside the wake has a higher frequency (smaller scale turbulence) compared to the undisturbed flow outside the wake above the deck.
7. The vertical scanning pattern demonstrates that the correlation can become strongly negative for certain separations when both points are within the wake zone. The correlation between observation points along the deck-parallel scanning line follows a traditional pattern of gradually reduced correlation values for increased separations. However, for the maximum 20 m separation, the correlation coefficient is still around 0.5.
8. The disturbed and undisturbed regions of the wake flow can be distinguished by looking at the Co-coherence, as negative and positive co-coherences are seen at low frequencies for wake-embedded and wake-free regions on the scanning line, respectively.

In summary, the lidar observations show noteworthy capabilities of

remote sensing for 3D wind field identification within any allowable distance of the short-range lidars. Future work will focus on expanding the current findings through further analysis of the available data.

## Declaration of competing interest

The authors declare that they have no known competing financial interests or personal relationships that could have appeared to influence the work reported in this paper.

## Acknowledgement

This work has received funding from the European Union Horizon 2020 through the Innovation Training Network Marie Skłodowska-Curie Actions: Lidar Knowledge Europe (LIKE (grant no. 858358)) and Marine Renewable Infrastructure Network for Enhancing Technologies 2, H2020, (MARINET2 (Grant no. 31084)). We would like to acknowledge the contributions of Michael Courtney, Per Hansen, Claus Brian Munk Pedersen (Technical University of Denmark), Swen Romer (University of Stavanger), and the Norwegian Public Road Administration (NPRA) in planning and conducting the measurement campaign.

## References

- Angelou, N., Foroughi Abari, F., Mann, J., Mikkelsen, T., Sjöholm, M., 2012a. Challenges in noise removal from Doppler spectra acquired by a continuous-wave lidar. In: Proceedings of the 26th International Laser Radar Conference.
- Angelou, N., Mann, J., Sjöholm, M., Courtney, M., 2012b. Direct measurement of the spectral transfer function of a laser based anemometer. *Rev. Sci. Instrum.* 83 (3).
- Angelou, N., Mann, J., Dellwik, E., 2021. Scanning Doppler lidar measurements of drag force on a solitary tree. *J. Fluid Mech.* 917.
- Carter, G., Knapp, C., Nuttall, A., 1973. Estimation of the magnitudesquared coherence function via overlapped fast Fourier transform processing. *IEEE Trans. Electroacoust. Audio* 21 (4), 337–344.
- Chapra, S.C., Canale, R.P., 2010. *Numerical Methods for Engineers*. McGraw Hill.
- Chen, W.-L., Li, H., Hu, H., 2014. An experimental study on the unsteady vortices and turbulent flow structures around twin-box-girder bridge deck models with different gap ratios. *J. Wind Eng. Ind. Aerod.* 132, 27–36.
- Cheyne, E., Jakobsen, J.B., Snæbjörnsson, J.T., 2016a. Buffeting response of a suspension bridge in complex terrain. *Eng. Struct.* 128, 474–487.
- Cheyne, E., Jakobsen, J.B., Snæbjörnsson, J.T., Mikkelsen, T., Sjöholm, M., Mann, J., Hansen, P., Angelou, N., Svardal, B., 2016b. Application of short-range dual-Doppler lidars to evaluate the coherence of turbulence. *Exp. Fluids* 57.
- Cheyne, E., Jakobsen, J.B., Snæbjörnsson, J.T., Angelou, N., Mikkelsen, T., Sjöholm, M., Mann, J., Svardal, B., 2017a. Full-scale observation of the flow downstream of a suspension bridge deck. *J. Wind Eng. Ind. Aerod.* 171, 261–272.
- Cheyne, E., Jakobsen, J.B., Snæbjörnsson, J.T., Reuder, J., Kumer, V., Svardal, B., 2017b. Assessing the potential of a commercial pulsed lidar for wind characterisation at a bridge site. *J. Wind Eng. Ind. Aerod.* 161, 17–26.
- Cheyne, E., Jakobsen, J.B., Snæbjörnsson, J.T., Mann, J., Courtney, M., Lea, G., Svardal, B., 2017c. Measurements of surface-layer turbulence in a wide Norwegian fjord using synchronized long-range Doppler wind LiDARs. *Rem. Sens.* 9, 977.
- Cheyne, E., Jakobsen, J.B., Snæbjörnsson, J.T., 2019. Flow distortion recorded by sonic anemometers on a long-span bridge: towards a better modelling of the dynamic wind load in full-scale. *J. Sound Vib.* 450, 214–230.
- Cheyne, E., Liu, S., Ong, M.C., Jakobsen, J.B., Snæbjörnsson, J.T., 2020. The influence of terrain on the mean wind flow characteristics in a fjord. *J. Wind Eng. Ind. Aerod.* 205.
- Daniotti, N., 2022. Bridge Deck Aerodynamics: A Case Study in Full Scale. PhD Thesis. University of Stavanger, Stavanger.
- Davenport, A., 1961. The spectrum of horizontal gustiness near the ground in high winds. *Q. J. R. Meteorol. Soc.* 87 (372), 194–211.
- Fu, W., Peña, A., Mann, J., 2022. Turbulence statistics from three different nacelle lidars. *Wind Energy Sci.* 7 (2), 831–848.
- Fuertes, F.C., Iungo, G.V., Porté-Agel, F., 2014. 3D turbulence measurements using three synchronous wind lidars: validation against sonic anemometry. *J. Atmos. Ocean. Technol.* 31 (7), 1549–1556.
- Guo, F., Mann, J., Peña, A., Schlipf, D., Cheng, P.W., 2022. The space-time structure of turbulence for lidar-assisted wind turbine control. *Renew. Energy* 195, 293–310.
- Hansen, S.O., 2021. Lysefjord bridge norway: static wind tunnel tests. SOH Wind Eng.
- Kuroda, S., 1997. Numerical simulation of flow around a box girder of a long span suspension bridge. *J. Wind Eng. Ind. Aerod.* 67–68, 239–252.
- Lange, J., Mann, J., Angelou, N., Berg, J., Sjöholm, M., Mikkelsen, T., 2016. Variations of the wake height over the Bolund escarpment measured by a scanning lidar. *Boundary-Layer Meteorol.* 159, 147–159.
- Li, H., Laima, S., Qiangqiang, Z., Li, N., Liu, Z., 2014. Field monitoring and validation of vortex-induced vibrations of a long-span suspension bridge. *J. Wind Eng. Ind. Aerod.* 124, 54–67.

- Lu, Q., Jin, Z., Wei, Z., 2020. Quantification of fatigue damage for structural details in slender coastal bridges using machine learning-based methods. *J. Bridge Eng.* 25 (7).
- Mann, J., Cariou, J.-P., Courtney, M.S., Parmentier, R., Mikkelsen, T., Wagner, R., Lindelöw, P., Sjöholm, M., Enevoldsen, K., 2009. Comparison of 3D turbulence measurements using three staring wind lidars and a sonic anemometer. *Meteorol. Z.* 18 (2), 135–140.
- Mikkelsen, T., 2009. On Mean wind and turbulence profile measurements from ground-based wind lidars: limitations in time and space resolution with continuous wave pulsed lidar systems. In: European Wind Energy Conference and Exhibition.
- Mikkelsen, T., Sjöholm, M., Angelou, N., Mann, J., 2017. 3D WindScanner lidar measurements of wind and turbulence around wind turbines, buildings and bridges. In: First Conference of Computational Methods in Offshore Technology (COTech2017), Stavanger.
- Miyata, T., Yamada, H., Katsuchi, H., Kitagawa, M., 2002. Full-scale measurement of Akashi-Kaikyo bridge during typhoon. *J. Wind Eng. Ind. Aerod.* 90 (12–15), 1517–1527.
- Nafisifard, M., Jakobsen, J.B., Cheynet, E., T, S.J., Sjöholm, M., Mikkelsen, T., 2021. Dual lidar wind measurements along an upstream horizontal line perpendicular to a suspension bridge. *IOP Conf. Ser. Mater. Sci. Eng.* 1201, 012008. <https://doi.org/10.1088/1757-899X/1201/1/012008>.
- Nafisifard, M., Pathan, S., Jakobsen, J.B., Sjöholm, M., Zasso, A., Giappino, S., Snæbjörnsson, J.T., Mann, J., 2023a. Observation of Flow Downstream of a Bridge Deck Model Using Cobra Probe and Lidars. Article (in press).
- Nafisifard, M., Jakobsen, J.B., Snæbjörnsson, J.T., Sjöholm, M., Mann, J., 2023b. Lidar measurements of wake around a bridge deck. In: 8th European-African Conference on Wind Engineering, Bucharest.
- Nafisifard, M., Jakobsen, J.B., Snæbjörnsson, J.T., Sjöholm, M., Mann, J., 2023c. Triple-lidar measurements of wind across a virtual rotor plane over a sea surface. *J. Phys. Conf. Ser.* (Accepted for publication).
- Pearson, R.K., 2005. *Mining Imperfect Data: Dealing with Contamination and Incomplete Records*. Society for Industrial and Applied Mathematics (SIAM).
- Puccioni, M., Iungo, G.V., Moss, C., S Solari, M., Letizia, S., Bodini, N., Moriarty, P., 2023. LiDAR measurements to investigate farm-to-farm interactions at the AWAKEN experiment. *J. Phys. Conf. Ser.* 2505, 012045. <https://doi.org/10.1088/1742-6596/2505/1/012045>.
- Sebastiani, A., Peña, A., Troldborg, N., Forsting, A.M., 2022. Evaluation of the global-blockage effect on power performance through simulations and measurements. *Wind Energy Sci.* 7 (2), 875–886.
- Sjöholm, M., Mikkelsen, T., Mann, J., Enevoldsen, K., Courtney, M., 2009. Spatial averaging-effects on turbulence measured by a continuous-wave coherent lidar. *Meteorol. Z.* 18 (3), 281–287.
- Sjöholm, M., Angelou, N., Hansen, P., Hansen, K.H., Mikkelsen, T., Haga, S., Silgjerd, J. A., Starsmo, N., 2014. Two-dimensional rotorcraft downwash flow field measurements by lidar-based wind scanners with agile beam steering. *J. Atmos. Ocean. Technol.* 31 (4), 930–937.
- Snæbjörnsson, J.T., Jakobsen, J.J., Cheynet, E., Wang, J., 2017. Full-scale monitoring of wind and suspension bridge response, 2017, Stavanger. In: 1st Conference of Computational Methods in Offshore Technology. COTech.
- Tamura, Y., Kareem, A., 2013. *Advanced Structural Wind Engineering*. Springer.
- Toriumi, R., Katsuchi, H., Furuya, N., 2000. A study on spatial correlation of natural wind. *J. Wind Eng. Ind. Aerod.* 87 (2–3), 203–216.
- Welch, P., 1967. The use of fast Fourier transform for the estimation of power spectra: a method based on time averaging over short, modified periodograms. *IEEE Trans. Audio Electroacoust.* 15 (2), 70–73.
- Yang, Y., Zhou, R., Ge, Y., Mohotti, D., Mendis, P., 2015. Aerodynamic instability performance of twin box girders for long-span bridges. *J. Wind Eng. Ind. Aerod.* 145, 196–208.
- Zhang, G., Liu, Y., Liu, J., Lan, S., Yang, J., 2022. Causes and statistical characteristics of bridge failures: a review. *J. Traffic Transport. Eng.* 9 (3), 388–406.